

Myopic exoplanet detection algorithm based on an analytical model of AO-corrected coronagraphic multi-spectral imaging

Marie Ygouf^{123a}, Laurent M. Mugnier¹³, David Mouillet²³, Thierry Fusco¹³, and Jean-Luc Beuzit²³

¹ ONERA - The French Aerospace Lab
F-92322 Châtillon, France

² UJF-Grenoble 1 / CNRS-INSU, Institut de Planétologie et d'Astrophysique de Grenoble (IPAG)
UMR 5274,

Grenoble, F-38041, France

³ GIS PHASE

Abstract. High contrast imaging for the detection and characterisation of exoplanets rests upon the instrument's capability to cancel the light of the host star. Unfortunately the combination of adaptive optics and coronagraphy is not sufficient: the residual starlight, or speckle noise, may be relatively bright compared to the signal of the planet and limits the detection sensitivity. These speckles find their origin in wavefront errors created by imperfections in the optical components. As they evolve on various time scales, calibrating these speckles out is very tricky and the suppression of the unavoidable residual speckle noise must be done by post-processing methods. The current empirical post-processing methods for calibrating out the residual speckles and detecting the potential exoplanets are not sufficient with respect to the specifications to be reached by the new and future generations of instruments. In this communication, we develop, in a bayesian framework, an inversion method that is based on an analytical imaging model. The model links the instrumental aberrations to the speckle pattern on the image focal plane, distinguishing between aberrations upstream and downstream of the coronagraph. This approach allows us to estimate both the speckles and the object map using the fact that the object does not scale with the wavelength as the speckle pattern does. We validate this method on realistic images with simulation conditions typical of a SPHERE-like instrument. We assess the performance of the method for different contrasts between the star and the planet flux.

1 Introduction

Ground-based instruments have now demonstrated the capability to detect planetary mass companions [1, 2] around bright host stars. By combining an adaptive optics (AO) system and coronagraphs, some first direct detections from the ground have been possible in favorable cases, at large separations and in young systems when low mass companions are still warm (≥ 1000 K) and therefore not too faint. There is a very strong astrophysical case to improve the high contrast detection capability (10^5 for a young giant planet to 10^{10} for an earth-like planet in the near infrared) very close to stars ($0.1''$ to $1''$).

Several instruments will be capable of performing multispectral imaging and will allow characterizing the planets by measuring their spectra. It is the case of GPI (Gemini) [3], Palm 3000 (Palomar) [4], SPHERE (VLT) [5] and several others that will follow. By combining an extreme adaptive optics (Ex-AO) and more accurate coronagraphs than before, the level of star light cancellation is highly improved, leading to a better signal to noise ratio. Yet, the residual host star light is affected by the instrument aberrations to form a pattern of intensity variations or "speckle noise" on the final image. Part of the speckles cannot be calibrated as they evolve on various time scales (neither fast enough to smooth down a halo nor stable enough) and for this reason, these "quasi-static speckles" are one of the main limitations for high contrast imaging.

A number of authors have discussed the challenge posed by the elimination of speckle noise in high contrast multispectral images. Some of these methods use the wavelength dependence of the speckle pattern to estimate it and subtract it from the image, while preserving both the flux and spectrum of the planet. Sparks and Ford (2002) were the first to describe the so-called "spectral deconvolution"

^a marie.ygouf@onera.fr

method in the framework of space-based observations for an instrument combining a coronagraph and an integral-field spectrometer (IFS) [6]. The method is entirely based on a speckle intensity fit by low-order polynomials as a function of wavelength, in the focal plane. But preserving the planet signals from being eliminated with the speckles is challenging because the planet presence is not explicitly modeled. Besides, some information on the measurement system can be very useful to disentangle a planet from the speckle field. Burke et al. (2010) combined classical empirical techniques of differential imaging with a multi-wavelength *phase retrieval* method to estimate the aberration pattern in the pupil plane with a simple imaging model without a coronagraph [7]. The inversion algorithm is based on a maximum-likelihood estimator, which measures the discrepancy between the data and an imaging model. In the present case, Burke’s wavelength diversity method does not apply readily, as it assumes non coronagraphic imaging, whereas we consider the highly non-linear case of a coronagraphic imaging model.

That is why we propose to take advantage of a combined use of wavelength diversity and a Bayesian inversion to jointly estimate the aberrations in the pupil plane and the planet map. The joint estimation aims at taking up the challenge of preserving the planets signal. An advantage of the Bayesian inversion is that it can potentially include an important regularization diversity to constrain the problem, using for example prior information on the noise, the planet map (position, spectrum, ...) or the aberrations. In the Bayesian framework, the criterion to be minimized is the sum of two terms: the data fidelity term, which measures the distance between the data and the imaging model, and one or some penalty terms. An important difficulty is to define a realistic coronagraphic imaging model which depends on parameters (aberrations...) that can be either calibrated beforehand or estimated from the data.

2 Parametric model of multi-spectral coronagraphic imaging

In order to carry out the Bayesian inverse problem method, we need to derive a parametric direct model of coronagraphic imaging. We assume that, for an AO-corrected coronagraphic image at the wavelength λ , the direct model is the following sum of three terms, separating the residual coronagraphic stellar halo, the circumstellar source (for which the impact of coronagraph is neglected) and noise n_λ : $i_\lambda(\alpha) = f_\lambda^* \cdot h_\lambda^c(\alpha) + [o_\lambda \star h_\lambda^{nc}](\alpha) + n_\lambda(\alpha)$, where the data are: $i_\lambda(\alpha)$, the image we have access to, f_λ^* is the star flux and $h_\lambda^{nc}(\alpha)$, the non-coronagraphic point spread function (PSF) which can be estimated separately. Solving the inverse problem is finding the unknowns: the object $o_\lambda(\alpha)$ and the speckle field $h_\lambda^c(\alpha)$ which we also call the “coronagraphic PSF”.

A model description of $h_\lambda^c(\alpha)$ directly depends on the turbulence residuals and optical wave front errors. Sauvage et al. (2010) proposed an analytical expression for coronagraphic image with a distinction between upstream and downstream aberrations [8]. The considered optical system is composed of a telescope, a perfect coronagraph and a detector plane. Some residual turbulent aberrations $\delta_r(\rho, t)$ are introduced in the telescope pupil plane. $\delta_r(\rho, t)$ is assumed to be temporally zero-mean, stationary, ergodic. Because we consider only long exposure time with respect to turbulence timescales, these turbulent aberrations contribute only through their spatial statistical properties: power spectral density $S_{\delta_r}(\alpha)$ or structure function D_{ϕ_r} . The static aberrations are separated into two contributions: the aberrations upstream of the coronagraph $\delta_u(\rho)$, in the telescope pupil plane $\mathcal{P}_u(\rho)$ and the aberrations downstream of the coronagraph $\delta_d(\rho)$ in the Lyot Stop pupil plane $\mathcal{P}_d(\rho)$. The perfect coronagraph is defined as an optical device that subtracts a centered Airy pattern of maximal energy to the electromagnetic field. Finally, the “coronagraphic PSF” depends on three parameters which define our system: the aberrations maps δ_u , δ_d and D_{ϕ_r} .

Derivation of an approximate long exposure “coronagraphic PSF” model Assuming that all the phases are small and that the spatial mean of $\phi_u(\rho)$ and $\phi_d(\rho)$ are equal to zero on the aperture, we derive a second-order Taylor expansion of expression 24 of [8]:

$$[h_\lambda^c]^{app}(\alpha) \simeq \left(\frac{2\pi}{\lambda}\right)^2 \left\{ \left| \mathcal{P}_d(\lambda\rho) \star \delta_u(\lambda\rho) \right|^2 \right\} + \left(\frac{2\pi}{\lambda}\right)^2 \left\{ \left| \mathcal{P}_d(\lambda\rho) \right|^2 \star S_{\delta_r}(\alpha) - \left\langle \left| P[\delta_r(\lambda\rho, t)] \right|^2 \right\rangle_t \cdot \left| \mathcal{P}_d(\lambda\rho) \right|^2 \right\}, \quad (1)$$

where $\widetilde{\mathcal{P}_d(\lambda\rho)}$ and $\widetilde{\delta_u(\lambda\rho)}$ are the Fourier transforms of the downstream pupil and upstream aberrations respectively and $P[\delta_r(\lambda\rho, t)]$ denotes the piston of the aberration map $\delta_r(\lambda\rho, t)$. $\left\{ \left\langle \left| P[\delta_r(\lambda\rho, t)] \right|^2 \right\rangle_t \cdot \left| \widetilde{\mathcal{P}_d(\lambda\rho)} \right|^2 \right\}$ is a corrective term that compensates for the fact that $\delta_r(\lambda\rho, t)$ is stationary and thus non-piston-free on the aperture at every instant. Note that $\left| \widetilde{\mathcal{P}_d(\lambda\rho)} \right|^2$ is the Airy pattern formed by the pupil $\mathcal{P}_d(\lambda\rho)$. This approximate expression brings physical insight to the Sauvage et al. expression:

- The speckle patterns scales radially in λ and evolves in $1/\lambda^2$ in intensity in the data cube. It is consistent with the analysis of Sparks and Ford [6], who perform fits of low-order polynomials as a function of the wavelength after rescaling radially.
- The approximate expression can be separated into one static term and one turbulent term. The turbulent term is simply the turbulent aberration power spectral density, as seen at the resolution of the instrument, i.e., convolved by the output pupil Airy pattern. The static term is directly function of the upstream aberrations.
- The downstream aberrations do not appear in the static term. This confirms that the role of the aberrations upstream and downstream of the coronagraph is very different and that upstream aberrations are dominant in the final image.
- Four equivalent upstream aberration sets: $\delta_u(\rho)$, $\delta_u(-\rho)$, $-\delta_u(\rho)$ and $-\delta_u(-\rho)$, that we call “quasi-equivalent” aberration maps, lead to the same image. This is further discussed in Section 3.3.

A study of this approximate model [9] showed that the image simulated with the approximate model is too different from the one simulated with the Sauvage et al. expression: the computation of the root mean square of the difference between the two images leads to an error of 29%. Consequently, even if using the approximate model would considerably decrease the non-convexity of the criterion, it would probably not lead to sufficiently good results. Nevertheless, and we will discuss this in Section 3, this approximate model will be useful to improve the convergence of our criterion minimization, which is a highly critical point.

Assumptions on the long exposure “coronagraphic PSF” model The information we get from the approximate model study helps us define some key assumptions for the success of the speckle field estimation with the Sauvage et al.’s long exposure “coronagraphic PSF” model. As they have a quite different impact on the final image, it is important to distinguish the aberrations upstream and downstream of the coronagraph. The downstream aberrations effect is lower than that of the upstream aberrations and furthermore, in foreseen systems, they are expected to be much more stable and easier to calibrate than upstream aberrations. Besides, as we consider long exposure images, the residual turbulent aberrations will be averaged to form a smooth halo easily distinguishable from a planet. Furthermore, the statistical quantity D_{ϕ_r} , which characterizes this halo, will be measured through the adaptive optics system wavefront sensor. Thus, in this paper, we assume that both the static downstream aberrations and the residual turbulent aberrations are calibrated and known. This decreases the number of unknowns as the only aberration map to estimate in order to get access to the “coronagraphic PSF” is the quasi-static upstream aberrations. We shall thus denote the long exposure “coronagraphic PSF” by $h_\lambda^c(\delta_u; \delta_d, D_{\phi_r})$ instead of $h_\lambda^c(\delta_u, \delta_d, D_{\phi_r})$ to underline the fact that δ_d and D_{ϕ_r} are assumed to be known.

3 Joint estimation of wavefront and object algorithm and minimization strategy

3.1 Definition of the criterion to be minimized and joint estimation

Following the Bayesian inverse problem approach, solving the inverse problem consists in finding the unknowns, firstly the object characteristics $o(\alpha, \lambda) = \{o_\lambda(\alpha)\}_\lambda$, secondly the parameters of the

speckle field $h_\lambda^c(\delta_u; \delta_d, D_{\phi_r})$ and $f^*(\lambda) = \{f_\lambda^*\}_\lambda$, which are the most likely given the data and our prior information about the unknowns. This boils down to minimizing the following criterion:

$$J(o, f^*, \delta_u) = \sum_\lambda \sum_\alpha \frac{1}{2\sigma_{n,\lambda}^2(\alpha)} |i_\lambda - f_\lambda^* \cdot h_\lambda^c(\delta_u; \delta_d, D_{\phi_r}) - o_\lambda \star h_\lambda^{nc}(\delta_u; \delta_d, D_{\phi_r})|^2(\alpha) + R_o + R_{f^*} + R_\delta + \dots \quad (2)$$

This criterion is the sum of two terms: the data fidelity term, which measures the distance between the data and the imaging model, and a non-exhaustive list of regularization terms on our unknowns R_o, R_{f^*}, R_δ . The noise variance $\sigma_{n,\lambda}^2$ is assumed to be known. The star flux at each wavelength can be analytically estimated from the criterion provided the regularization on flux is quadratic or absent.

The structure of the criterion of Eq. (2) prompted us to adopt a joint estimation of wavefront and object with an iterative algorithm, which alternates between estimation of the aberrations, assuming that the object is known (multispectral *phase retrieval*) and estimation of the object assuming that the aberrations are known (*non-myopic multispectral deconvolution*).

3.2 Non-myopic multispectral deconvolution

The *non-myopic multispectral deconvolution* is relatively well-known. The chosen regularization leads to a convex criterion and thus to a unique solution for a given set of aberrations.

The regularization term R_o includes prior spatial and spectral information we have on the object. We chose here a L1-L2 white spatial regularization which assumes the independence between the pixels [10] because we are mainly looking for point sources. The spectral prior is based on the object spectrum smoothness. We currently assume that the object is white (constant spectrum) but as the final aim is to extract some spectra, for future validations we will use a L2 correlated spectral regularization [11] which will involve at each pixel the differences between the spectrum at neighboring wavelengths and will enforce smoothness on the object spectrum.

3.3 Phase retrieval: dealing with local minima

Choice of an appropriate starting point: very small random phase In order to keep the computation time reasonable, we use a local descent algorithm to minimize the criterion. Because the latter is highly non-convex, the chosen starting point can lead or not to the global minimum of the criterion. The solution is brought by assuming that the upstream aberrations are small enough at the starting point so that we are fully in the conditions where the Taylor expansion developed in [9] is valid and where the criterion is less non-convex. It allows the algorithm to avoid many wrong directions, and thus many local minima. As the algorithm converges, the upstream aberration rms value increase towards their true value and a gradual non-linearity of the model is little by little introduced.

Choosing an aberration map with a small rms value as a starting point of the *phase retrieval* allows us to avoid some local minima by linearizing the highly non-convex model used in the inversion.

Avoiding some local minima by testing quasi-equivalent starting points In the approximate model, four different aberration maps can give the same image (cf. Section 2). This means that, from a given starting point, the minimization algorithm can take four different but equivalent directions from the approximate model point of view. But from the point of view of the model used in the inversion [8], it is not the case because it depends on downstream aberrations, which break the symmetry.

Consequently, a good solution from the point of view of the approximate model may be a not-so-good one from the model used in the inversion point of view. The idea is then to perform an initialization step where the very small random phase is taken as a starting point. A first *phase retrieval* stage is performed with this starting point, leading to a first estimated aberration map denoted by $\delta_u^{init,1}(\rho)$. Then, the three other quasi-equivalent aberration maps $\delta_u^{init,1}(-\rho)$, $-\delta_u^{init,1}(\rho)$ and $-\delta_u^{init,1}(-\rho)$ are taken as starting points for three other *phase retrieval* stages. This leads to three more estimated aberration maps denoted by $\delta_u^{init,2}$, $\delta_u^{init,3}$ and $\delta_u^{init,4}$.

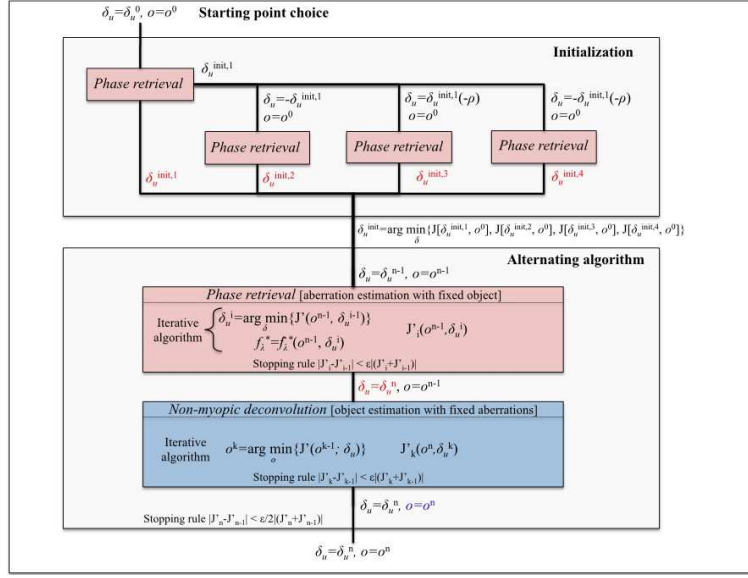


Fig. 1. Block diagram of the algorithm used for the jointly estimation of the object map and static upstream aberrations.

Avoiding some local minima in the multispectral inversions by taking the previously estimated aberration map as starting point In spite of setting up solutions in order to avoid the local minima while the minimization criterion, we sometimes observe some minimization difficulties in the case of inversions with more than two spectral channels. The reason of this problem has not been identified. That is why we begin to do an inversion with one spectral channel. Then, we add one spectral channel for a two-spectral channel inversion and we take the previous estimated aberration map as a starting point. Doing this when adding some more spectral channels is a way of constraining the problem, waiting for understanding the reason of these minimization difficulties.

3.4 Summary of the developed algorithm

Figure (1) summarizes the different steps of the developed algorithm. The choice of a very small random phase as a starting point is essential because it avoids falling into some local minima (section 3.3). An initialization phase is performed, testing the algorithm convergence for the four quasi-equivalent solutions (section 3.3). The solution which leads to the smallest criterion value is selected. Then, the minimization core is performed, alternating between the aberration estimation, assuming that the object is known (multispectral *phase retrieval*, section 3.3), and the object estimation, assuming that the aberrations are known (*non-myopic multispectral deconvolution*, section 3.2). Several iterations are performed until the stopping rule of the algorithm is verified.

4 Validation of the inversion method by simulations

Test case: Data processing with “SDI” From a data cube of six images simulated with the image formation model of Section 2 and the Sauvage et al. [8] analytical expression of coronagraphic imaging, we jointly estimate the speckle field and the object map. The simulated instrumental conditions are typical of a SPHERE-like instrument and the same as these of Ygouf et al. [13]: upstream δ_u and downstream δ_d aberrations respectively simulated with standard deviation of 30 nm and 97 nm, star-planet angular separations of 0.2 and 0.4 arcsec, contrasts, i.e. ratio of star flux over planet flux of 10^5 ,

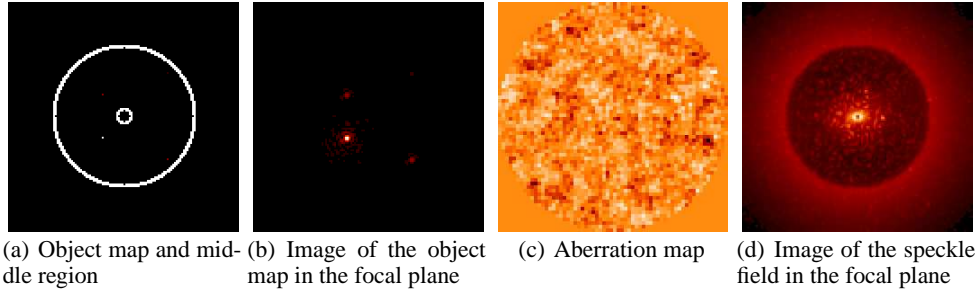


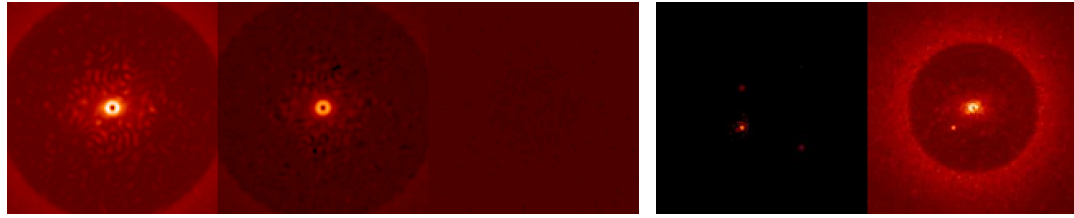
Fig. 2. Simulated images at $\lambda = 950$ nm. (a) Simulated object map and (b) associated image in the focal plane. The image is obtained by convolving the object map o_λ by the non-coronagraphic psf h_λ^{nc} . (c) Simulated aberrations and (d) associated image of the speckle field in the image focal plane. The image is given by the “coronagraphic PSF” h_λ^c .

10^6 and 10^7 , a [950 nm ; 1647 nm] spectral bandwidth and a maximum flux per pixel of 10^8 on the data cube in presence of photon noise corresponding to the observation of a 6-magnitude star for 30 minutes with the VLT.

Figure (2) shows the simulated objet map (2(a)) and the associated image in the focal plane (2(b)). Figure 2 shows the simulated aberration map (2(d)) and the associated image of the speckle field in the focal plane (2(d)). In the following, we focus on the middle region defined in Figure (2(a)). Materialized by the two white circles, this is a ring from 2 to 20 λ/D which corresponds to angular distances between $\simeq 0,05''$ and $\simeq 0,5''$ at 950 nm. In this region, the adaptive optics compensates for the turbulent aberrations. Quasi-static aberrations are dominant, thus they limit the detection. For this reason, this is the region which interests us the most to study the convergence capabilities of our algorithm.

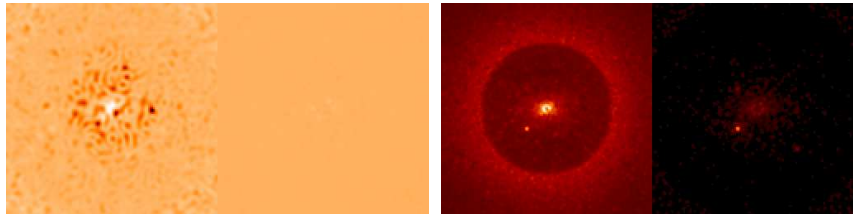
We process the simulated images with an optimized “SDI” in order to have a comparison point to estimate the performance of our method. We compare quantitatively the stellar residuals which will limit the detection capability, after post-processing. To do this, we consider the two following bandwidths: [950 nm ; 1650 nm] and [950 nm ; 1150 nm]. The first bandwidth is typical of an IFS-SPHERE-like instrument but this spectral separation is not favorable to the SDI. The second bandwidth is closer to separations we have when using differential filters. For each bandwidth, we take the images at the minimum and maximum wavelengths and we rescale the image at 950 nm with respect to the images at 1150 nm and 1650 nm. Finally, we perform the following spectral differences between the two images: $i_{\text{diff}_{1650}} = i_{1650 \text{ nm}} - \gamma i_{950 \text{ nm}}$ and $i_{\text{diff}_{1150}} = i_{1150 \text{ nm}} - \gamma i_{950 \text{ nm}}$, where γ is a coefficient which minimize the squared difference $|i_{\text{max}} - \gamma i_{\text{min}}|^2$ on the middle region $m(\rho)$. γ is the coefficient that minimized the squared difference on this region and is given by [12]: $\gamma = \frac{\sum_\rho m(\rho) i_{950 \text{ nm}}(\rho) i_{1650 \text{ nm}}(\rho)}{\sum_\rho m(\rho) i_{1650 \text{ nm}}^2(\rho)}$, where m is a mask that is equal to 1 on the pixels belonging to the middle region and 0 elsewhere. This two-channel subtraction reduces the level of stellar halo by a factor 10 (resp 4) in the middle region for the bandwidth [950 nm ; 1150 nm] (respectively [950 nm ; 1650 nm]).

Inversion with only one spectral channel We jointly estimate the upstream quasi-static aberration map and the object map with only one spectral channel at 950 nm. Figure (3(a)) compares the residual speckles in the focal plane after post-processing with the “optimized” SDI method and our method, with respect to the image before post-processing. The inversion with only one spectral channel allows a 81-fold gain to the speckle subtraction, in the middle region defined in Figure (2(a)). Figure (3(b)) compares the estimated object image in the focal plane (right) to the simulated one (left). Even if many residuals from the turbulent halo and residual speckles subsist on the object image, one of the planets, that with a contrast of 10^5 , is detected at the right position. This result shows our algorithm convergence capability in spite of the degeneracy difficulties and the presence of local minima.



(a) **Speckle fields.** With the same dynamic, at 1650 nm: (left) image before post-processing and (middle) speckle residuals after post-processing with (middle) SDI and with (right) a one-spectral channel inversion. For visualization reasons, the last image was rescaled from 950 nm to 1650 nm.
 (b) **Images of object.** With the same dynamic, at 950 nm: (left) simulated and (right) estimated planet image $[o_\lambda \star h_\lambda^{nc}](x, y)$ with a one-spectral channel inversion.

Fig. 3. Inversion with one spectral channel.



(a) **Speckle fields.** Speckle residuals after post-processing, with the same dynamic: (left) inversion with one spectral channel and (right) two spectral channels.
 (b) **Images of object.** Simulated (left) and estimated planets images $[o_\lambda \star h_\lambda^{nc}](x, y)$, at 950 nm with the same dynamic: (middle) inversion with one spectral channel and (right) two spectral channels.

Fig. 4. Inversion with multispectral data cubes.

Inversion with multispectral data cubes We jointly estimate the upstream quasi-static aberration map and the object map with multispectral data. The inversion is realized with two, three, four, five and six spectral channels taken in the simulated data cube of six images.

The speckle field estimation in the focal plane is improved with the multispectral inversion as shown in Figure (4(a)). The right image is the subtraction between the simulated speckle field and the estimated one, the former being the result of the inversion with two spectral channels. The inversion with two spectral channels allows a gain of a factor 2000 in the speckle subtraction in the middle region defined in Figure (2(a)).

Figure (4(b)) compares the estimated object image for inversions with one (left) and two (right) spectral channels. With two spectral channels, the two planets with a contrast of 10^6 are detected at the right position, in addition to the planet with a contrast of 10^5 . The planet with a contrast of 10^7 is not detected because it is flooded by the photon noise. The turbulent halo residuals in the final image, very strong with the one-image inversion, are attenuated by using more images for the inversion. The results with more spectral channels than two are not represented here because they lead to the same visual aspects as those with two spectral channels. The evolution of the rms value of the difference between the simulated and the estimated object images is represented in Figure (5), for all the images, in the middle region defined in Figure (2(a)). The rms value of the difference between the simulated and the estimated images decreases with the number of wavelengths used for the inversion. This confirms that adding some more wavelengths, thus more information, improves the joint estimation performance.

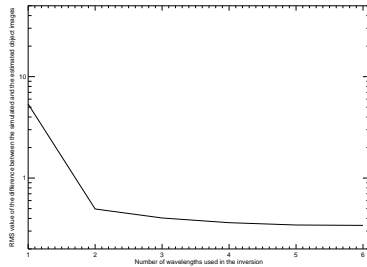


Fig. 5. Inversion with multispectral data cubes. Evolution of the rms value of the difference between the simulated and the estimated object images as a function of the number of spectral channels used in the inversion, in the middle region defined in Figure (2(a)).

5 Conclusion

We have proposed an original method of image restoration for the new generation of planet finders. For the first time, a fine parametric model of coronagraphic imaging, describing the instrument response, is used for the inversion of simulated multispectral images, in a solid statistical framework. The choice of a Bayesian approach allows to use a wide variety of prior information either about the system (aberrations, flux, noise) and about the object of interest. An interest of the method is the possibility of adjusting the weight of the prior information according to the instrumental aberrations and object knowledge and the instrument stability.

In order to set up this method, we have developed an iterative algorithm which estimates jointly the object (*non-myopic multispectral deconvolution*) and the aberrations (*multispectral phase retrieval*). Estimating the aberrations is a difficult issue because of the high non-linearity of the coronagraphic imaging analytical model and the number of unknowns to estimate (about 10^3 in our case). Nevertheless, we have demonstrated the convergence capabilities of the algorithm, by bringing original solutions to the minimization difficulties of the *phase retrieval*.

The restoration of images simulated with a perfect coronagraph is very encouraging for the extraction of planetary signals at levels beginning to be astrophysically interesting. We have demonstrated the efficiency of the method even with only one spectral channel, by achieving a contrast of 10^5 at 0.2 arcsec. Multispectral redundancy improves the detection as soon as we add one more spectral channel, allowing to achieve a contrast of 10^6 at 0.2 arcsec.

We thus believe that multispectral approach will be determining when we confront it with experimental data. This deserves to be studied, as well as how the performance will evolve in the different cases of images simulated with a non-perfect coronagraph, real images from the SPHERE instrument on lab or real images from an instrument on-sky.

References

1. A.-M. Lagrange et al., “A Giant Planet Imaged in the Disk of the Young Star β Pictoris,” *Science* **329** (2010).
2. C. Marois et al., “Direct Imaging of Multiple Planets Orbiting the Star HR 8799,” *Science* **322** (2008).
3. J. R. Graham et al., “Ground-Based Direct Detection of Exoplanets with the Gemini Planet Imager (GPI),” (2007).
4. S. Hinkley et al., “A New High Contrast Imaging Program at Palomar Observatory,” *Pub. Astron. Soc. Pacific* **123** (2011).
5. J.-L. Beuzit et al., “SPHERE: a planet finder instrument for the VLT,” in “Society of Photo-Optical Instrumentation Engineers (SPIE) Conference Series,” (2008).
6. W. B. Sparks et al., “Imaging Spectroscopy for Extrasolar Planet Detection,” *Astrophys. J.* **578** (2002).
7. D. Burke et al., “Enhanced faint companion photometry and astrometry using wavelength diversity,” *J. Opt. Soc. Am. A* **27** (2010).
8. J.-F. Sauvage et al., “Analytical expression of long-exposure AO-corrected coronagraphic image. First application to exoplanet detection,” *J. Opt. Soc. Am. A* (2010).
9. M. Ygouf et al., “Approximate analytical model of AO-corrected coronagraphic imaging, with a view to exoplanet detection and characterisation,” in “In the Spirit of Lyot 2010,” (2010).
10. S. Meimon et al., “Self-calibration approach for optical long-baseline interferometry imaging,” *J. Opt. Soc. Am. A* **26** (2008).
11. E. Thiébaud et al., “Maximum a posteriori planet detection and characterization with a nulling interferometer,” in “IAU Colloq. 200: Direct Imaging of Exoplanets: Science & Techniques,” (2006).
12. A. Cornia, “High-contrast differential image processing for extrasolar planet detection,” Ph.D. thesis, École Doctorale d’Astronomie et d’Astrophysique d’Île de France (2010).
13. M. Ygouf et al., “Simultaneous exoplanet detection and instrument aberration retrieval in multispectral coronagraphic imaging,” *Optics Express*, submitted.